

# Optical imaging with nanoscale resolution using optical nonlinearities and spatiotemporal modulation

D. D. Yavuz and Z. J. Simmons

*Department of Physics, 1150 University Avenue, University of Wisconsin at Madison, Madison, Wisconsin, 53706, USA*

(Received 1 June 2012; published 13 July 2012)

We suggest a type of imaging technique that uses optical nonlinearities and spatiotemporal modulation to achieve nanoscale resolution in the far field. The technique utilizes intense laser beams to produce an optical excitation with spatial features that are much smaller than the wavelength of light. Nonlinear mixing with the excitation can then be used to imprint the information contained in high spatial frequencies into the propagating region. As a specific example, we study the implementation of this technique using coherent anti-Stokes Raman scattering (CARS) near maximum molecular coherence. Our simulations suggest that it may be possible to resolve the structure of complex biological molecules at the nanometer scale in the far field using near-infrared light.

DOI: [10.1103/PhysRevA.86.013817](https://doi.org/10.1103/PhysRevA.86.013817)

PACS number(s): 42.65.Dr, 42.50.Gy, 42.30.Va

As the frontiers of science and technology approach the nanoscale, it has become ever more important to devise optical imaging techniques with nanometer resolution. It is well known that traditional imaging techniques cannot resolve features that are smaller than the wavelength of light. This is the diffraction limit, and overcoming this barrier has been the subject of intense theoretical and experimental research over the last two decades [1–7]. A simple and efficient optical technique that can resolve nanometer spatial scales will likely have significant implications for a number of research areas including biological imaging and nanotechnology. In this work, we describe a technique that utilizes saturation of optical nonlinearities and a specific type of spatiotemporal modulation to obtain nanoscale resolution. Our approach does not require a near-field scanning tip, and it achieves super-resolution in the far field using a relatively simple optical setup. Due to a nonlinear response, intense laser beams can produce an optical excitation with spatial features that are much smaller than the wavelength of light. The key idea is to use nonlinear mixing with this established excitation to mix down high spatial frequencies (spatial Fourier components). This mixing brings the high spatial frequencies, which normally produce only evanescent waves unavailable for imaging, into the propagating region. A type of spatiotemporal modulation is then used to recover the high spatial frequency components in the image plane. As a concrete example, we focus on implementing this approach using coherent anti-Stokes Raman scattering (CARS) near maximum molecular coherence. We perform numerical simulations of the density matrix for parameters that are typical of a biological molecule. Our simulations suggest that it may be possible to resolve the structure of complex biological molecules at the nanometer scale in the far field using near-infrared light.

Our approach builds upon a number of super-resolution concepts that have been discussed in the literature. Using saturation of the excited fluorescing level, the technique of stimulated emission depletion microscopy (STED) has recently achieved about 10 nm resolution in the far field [8–10]. The idea of mixing down high spatial frequencies has recently been demonstrated by the structured illumination technique

of biological imaging [11,12]. Utilizing advances in ultrafast lasers, CARS microscopy has evolved into a powerful imaging tool that does not require a fluorescent agent [13–16]. Various techniques for improving the resolution of CARS microscopy beyond the diffraction limit have recently been suggested [17–19]. Super-resolution using spatiotemporal modulation in laser scanning microscopy has recently been discussed [20]. Our approach improves on these pioneering efforts with the following key advantages: (i) Our technique does not require scanning of a tight spot. Super-resolution is achieved using a wide-field image, which considerably simplifies the experimental setup. (ii) We use a type of spatiotemporal modulation that produces radiation at different frequencies for different spatial Fourier domains. As a result, it becomes possible to retrieve all spatial frequencies simultaneously. (iii) Since we utilize a nonlinear optical response, our approach does not require a fluorescent agent. The scheme may therefore be implemented for a broad range of complex molecules.

We first discuss our approach in a general framework. The simplified setup is shown in Fig. 1(a). For simplicity, we will consider a two-dimensional object; that is, the object is assumed to have infinitesimal depth in the  $z$  direction. Suppose that we induce a dipole moment pattern  $\vec{\mu}$  in the object with very small spatial features. We work with phasor quantities and write the induced dipole moment in the form

$$\vec{\mu}(x, y, z, t) = \hat{e}_\mu \text{Re}\{\mu(x, y) \exp(-i\omega t)\} \delta(z - z_0), \quad (1)$$

where  $\hat{e}_\mu$  is the unit vector oriented along the dipole and  $z_0$  is the position of the object along the  $z$  axis. In Eq. (1), we have assumed monochromatic excitation (steady state) at frequency  $\omega$ . For excitation with pulsed laser beams of sufficient duration, as is the case in the numerical example that will be discussed below, the analysis can be extended to apply to the temporal peak of the pulses. We can decompose the induced dipole moment into its spatial Fourier components:

$$\mu(x, y) = \int_{-\infty}^{\infty} \int_{-\infty}^{\infty} A(k_x, k_y) \exp(ik_x x + ik_y y) dk_x dk_y. \quad (2)$$

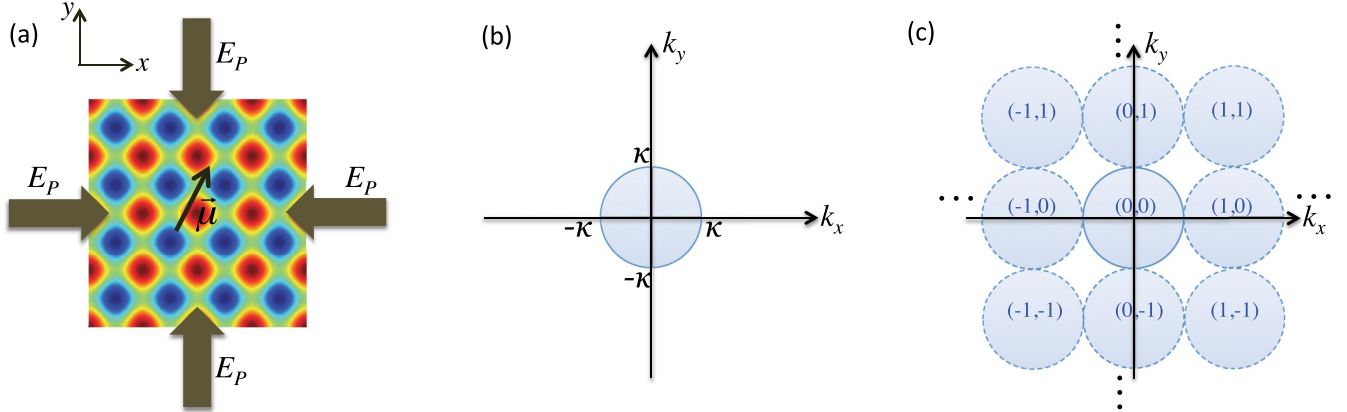


FIG. 1. (Color online) (a) Simplified schematic. The goal is to resolve with nanometer resolution a radiator with dipole moment  $\vec{\mu}$  in the far field. Two counterpropagating beam pairs form a standing wave intensity pattern in the two transverse directions  $x$  and  $y$  with a periodicity of  $\lambda/2$ . For sufficiently high pump laser intensity, the standing wave pattern may induce an excitation structure with spatial features that are much smaller than the periodicity of the pattern and thus the wavelength of the light. The nonlinear mixing of this excitation with the induced dipole results in the retrieval of the high spatial Fourier components in the far field. See text for details. (b) Pass band of traditional imaging techniques in Fourier space. Only spatial frequencies  $k_x^2 + k_y^2 < \kappa^2$  contribute to the far-field image. (c) Circular regions  $(l_x, l_y)$  in Fourier space that are defined by  $(k_x - 2l_x\kappa)^2 + (k_y - 2l_y\kappa)^2 < \kappa^2$ . The nonlinear interaction of the dipole with the pump beams mixes the high spatial frequency Fourier components down to the propagating range.

The dipole moment  $\vec{\mu}$  will radiate light and Eq. (2) can also be thought of as a plane wave decomposition of radiation at  $z = z_0$ , with wave-vector components  $k_x$ ,  $k_y$ , and  $k_z$ . From Maxwell's equations these components must satisfy  $k_x^2 + k_y^2 + k_z^2 = \kappa^2$ , where  $\kappa = 2\pi/\lambda$  and  $\lambda$  is the wavelength in free space. The diffraction limit is due to the fact that for  $k_x^2 + k_y^2 > \kappa^2$ ,  $k_z$  must be complex, and thus the resulting waves are evanescent along  $z$  and are therefore inevitably removed from the image. As a result, in the far field only Fourier amplitudes  $A(k_x, k_y)$  with  $k_x^2 + k_y^2 < \kappa^2$  contribute to the image. As shown in Fig. 1(b), with this in mind, we can view wave propagation as low-pass filtering of the spatial frequencies where the pass band is the circular region  $k_x^2 + k_y^2 < \kappa^2$ . High spatial frequency Fourier components outside of this propagating region are filtered out.

One of the key ideas of the technique is that, by using nonlinear mixing, high spatial frequencies can be “mixed down” into the propagating region [11,12]. Consider a nonlinear interaction of the radiating dipoles with a pump laser beam,  $E_P$ , that is split into two counterpropagating beam pairs to produce a two-dimensional standing wave intensity pattern  $I_P(x, y)$ . For simplicity, we will take the wavelength of the pump laser beam to be similar to the radiated wavelength,  $\lambda_P \approx \lambda$ . The standing-wave intensity pattern is periodic in each direction with a period of  $\lambda/2$  [i.e.,  $I_P(x + l_x\lambda/2, y + l_y\lambda/2) = I_P(x, y)$  for all integers  $l_x$  and  $l_y$ ]. Now assume that there is a nonlinear, intensity-dependent excitation due to the pump laser which we will denote by a general function  $f(I_P)$ . As we will discuss below, for the specific CARS scheme, the excitation will be the coherence of the molecular (vibrational or rotational) transition. Note that the function  $f$  will have the same periodicity of  $\lambda/2$  [i.e.,  $f(x + l_x\lambda/2, y + l_y\lambda/2) = f(x, y)$ ]. However, because the intensity dependence can be highly nonlinear, for sufficiently high pump laser intensities  $f(x, y)$  may have spatial features that are significantly sharper than those of the standing wave intensity pattern. Such excitation

localization has been discussed extensively in atomic physics literature [21–27] and has also been experimentally observed by a number of groups [28–31]. Because  $f$  is periodic, it will have a two-dimensional Fourier series expansion:

$$f(x, y) = \sum_{m=-\infty}^{\infty} \sum_{n=-\infty}^{\infty} c_{m,n} \exp(i2m\kappa x + i2n\kappa y). \quad (3)$$

Assume that we have a mixing nonlinearity that modulates the induced dipole moment with the function  $f$  to produce a new pattern  $\mu_{\text{new}} = f(x, y)\mu(x, y)$ . Using Eqs. (2) and (3), we have:

$$\begin{aligned} \mu_{\text{new}} = & \sum_{m=-\infty}^{\infty} \sum_{n=-\infty}^{\infty} c_{m,n} \int_{-\infty}^{\infty} \int_{-\infty}^{\infty} A(k_x, k_y) \\ & \times \exp[i(k_x + 2m\kappa)x + i(k_y + 2n\kappa)y] dk_x dk_y. \end{aligned} \quad (4)$$

Equation (4) indicates that high spatial Fourier components can be mixed down to the propagating region through multiplication with the appropriate Fourier series expansion term so that the resulting waves are no longer evanescent. Let us divide Fourier space into circular regions of radius  $\kappa$  for which  $(k_x - 2l_x\kappa)^2 + (k_y - 2l_y\kappa)^2 < \kappa^2$  for a given integer pair  $(l_x, l_y)$ , as shown in Fig. 1(c).  $(0,0)$  denotes the propagating region and all other regions  $(l_x, l_y)$  would normally produce evanescent waves. The high-frequency Fourier components  $A(k_x, k_y) \exp(ik_x x + ik_y y)$  in region  $(l_x, l_y)$  can be shifted to the propagating region through multiplication by  $c_{-l_x, -l_y} \exp(-i2l_x\kappa x - i2l_y\kappa y)$ . Only the components that have been shifted to the propagating region will contribute to the far field. Using Eq. (4), the far-field contribution can be written as a sum of integrals over the regions  $(l_x, l_y)$ , where each integral is shifted by the appropriate Fourier series expansion

term:

$$\begin{aligned} \mu_{\text{new}}^{\text{far field}} = & \sum_{l_x, l_y} c_{-l_x, -l_y} \iint_{(l_x, l_y)} A(k_x, k_y) \exp[i(k_x - 2l_x\kappa)x \\ & + i(k_y - 2l_y\kappa)y] dk_x dk_y. \end{aligned} \quad (5)$$

As shown in Fig. 1(c), this procedure misses the areas between the circular regions  $(l_x, l_y)$ , which cannot be moved into the propagating region using the multiplication scheme above. We note that the circular regions contain 78% of the area in Fourier space and as a result they may be sufficient to obtain a high-quality image. Furthermore, the missing regions can be recovered using a number of techniques. For example, one can rotate the axis of the pump beam standing wave pattern to a diagonal primed basis,  $x' = x + y$  and  $y' = x - y$ . This results in a subsequent rotation of the  $(l_x, l_y)$  regions of Fig. 1(c), placing them along the lines  $k_x = k_y$  and  $k_x = -k_y$  in Fourier space. If the complete image reconstruction procedure described below is repeated, this allows the retrieval of Fourier components that lie between the circular regions of Fig. 1(c).

Equation (5) indicates that the far field can, in principle, include contributions from all spatial frequencies (i.e., there is no low-pass filtering). We note, however, that the far-field contribution results from a complicated sum, and we have not yet addressed how to recover all of the Fourier components  $A(k_x, k_y)$  from such a sum. To accomplish this, we suggest using traveling wave modulation such that the intensity pattern for the pump laser beam is swept at speeds  $v_x$  and  $v_y$  in the two directions. As shown below, this type of spatiotemporal modulation can be used to recover individual terms in the summation of Eq. (5). Such modulation can be accomplished, for example, by having the counterpropagating pump beam pairs differ slightly in frequency. This would result in an excitation pattern that moves in the two directions,  $f(x - v_x t, y - v_y t)$ . The two-dimensional Fourier series expansion now reads

$$\begin{aligned} f(x - v_x t, y - v_y t) &= \sum_{m=-\infty}^{\infty} \sum_{n=-\infty}^{\infty} c_{m,n} \exp[i2m\kappa(x - v_x t) + i2n\kappa(y - v_y t)] \\ &= \sum_{m=-\infty}^{\infty} \sum_{n=-\infty}^{\infty} c_{m,n} \exp(-i2m\delta\omega_x t - i2n\delta\omega_y t) \\ &\quad \times \exp(i2m\kappa x + i2n\kappa y), \end{aligned} \quad (6)$$

where we have defined  $\delta\omega_x \equiv \kappa v_x$  and  $\delta\omega_y \equiv \kappa v_y$ . Equation (6) shows that each series expansion coefficient  $c_{m,n}$  becomes multiplied by a temporal factor (i.e., a temporal frequency shift). These temporal factors can be carried out through the whole formalism and Eq. (5) will then read

$$\begin{aligned} \mu_{\text{new}}^{\text{far field}} = & \sum_{l_x, l_y} c_{-l_x, -l_y} \exp(i2l_x\delta\omega_x t + i2l_y\delta\omega_y t) \\ & \times \iint_{(l_x, l_y)} A(k_x, k_y) \exp[i(k_x - 2l_x\kappa)x \\ & + i(k_y - 2l_y\kappa)y] dk_x dk_y. \end{aligned} \quad (7)$$

Equation (7) indicates that each of the terms in the summation are frequency shifted by an amount  $(2l_x\delta\omega_x + 2l_y\delta\omega_y)$ . As a

result, the Fourier component  $A(k_x, k_y)$  from each circular region  $(l_x, l_y)$  [corresponding to  $(k_x - 2l_x\kappa)^2 + (k_y - 2l_y\kappa)^2 < \kappa^2$ ] will be radiated at a slightly different temporal frequency (assigning a unique temporal frequency to each circular region requires the ratio  $v_x/v_y$  to be irrational). The individual terms in the summation of Eq. (7) may therefore be recovered using spectral techniques. One simple approach, for example, would be to use a grating and spatially separate these different components on the optical detector (for example, a CCD camera). The full image may then be recovered by appropriately combining the information from these different Fourier regions using a reconstruction algorithm. The complete reconstruction will require retrieving the phase as well as the amplitude of the Fourier components. To retrieve the phase, one approach would be, for example, to interfere the radiated light with a reference wave on the CCD. We note that the reconstruction does not necessarily require the precise knowledge of the Fourier series expansion coefficients  $c_{m,n}$ . Since most objects would produce a continuous and relatively smooth spectrum, one approach would be to scale the signal levels from the circular regions so that the Fourier components at the boundaries would match.

We next focus on a concrete implementation of this approach using the Raman nonlinearity with the goal of extending the CARS imaging technique into the nanoscale regime. Over the last decade, CARS has evolved into a powerful technique for biological imaging and has recently been used to obtain images of tissues and living cells with about one micron resolution [13–16]. Consider a specific  $|a\rangle \rightarrow |b\rangle$  vibrational or rotational excitation of a molecule as shown in Fig. 2. Intense pump and Stokes laser beams,  $E_P$  and  $E_S$ , drive the coherence of the vibrational or rotational excitation,  $\rho_{ab}$ . The frequencies of the driving laser beams are tuned close to the Raman excitation frequency  $\omega_P - \omega_S \approx \omega_{ab}$ . A third laser beam, called the mixing beam  $E_M$ , may then mix with the established coherence and produce a nonlinear dipole moment at frequency  $\omega_G = \omega_P - \omega_S + \omega_M$ . The goal is to collect scattered light at frequency  $\omega_G$  due to the induced nonlinear dipole moment and super-resolve the locations of the vibrations or rotations (and therefore the structure of a complex molecule). We will take the mixing beam to be sufficiently weak so that it does not interfere with the preparation of the molecular coherence. Similar to the above discussion, we consider near-monochromatic excitation and write the dipole moment of the form  $\bar{\mu}_{\text{nonlinear}}(x, y, z, t) = \hat{e}_\mu \text{Re}\{\mu_{\text{nonlinear}} \exp(-i\omega_G t)\} \delta(z - z_0)$ . In the limit where the detunings  $\Delta_P$  and  $\Delta_M$  are much larger than all of the other rates in the problem, the population of the excited level  $|e\rangle$  can be algebraically evaluated, and the generated nonlinear dipole moment is [32,33]

$$\mu_{\text{nonlinear}} = \rho_{ab} \frac{\Omega_M}{2\Delta_M} \mu_{ae}, \quad (8)$$

where we have defined the corresponding Rabi frequency of the mixing beam as  $\Omega_M \equiv E_M \mu_{be}/\hbar$ . The quantities  $\mu_{ij}$  are the dipole matrix elements (i.e., the expectation values of the dipole moment operator) between levels  $i$  and  $j$ . Adopting a similar language to that of the above discussion, Eq. (8) can be thought of as the dipole moment of the two-level system which is spatially localized to the atomic

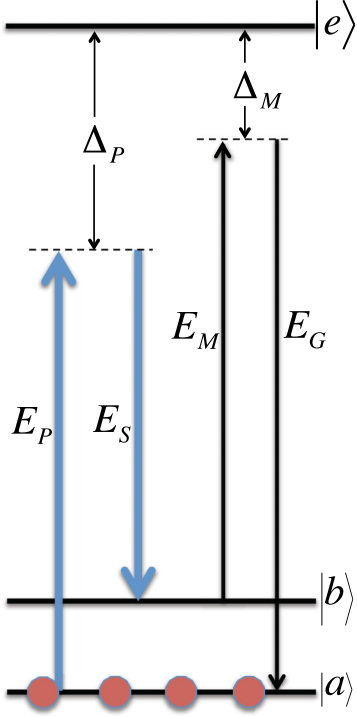


FIG. 2. (Color online) Energy level diagram for CARS technique near maximum coherence. Intense pump and Stokes laser beams,  $E_P$  and  $E_S$ , drive the coherence of the molecular transition,  $\rho_{ab}$ . A third laser beam,  $E_M$ , mixes with the established coherence and generates the wave  $E_G$  at frequency  $\omega_G = \omega_P - \omega_S + \omega_M$ . Driven near its maximum value  $\rho_{ab} = 0.5$ , the established molecular coherence may have spatial features much smaller than the wavelength of light.

scale,  $\mu_{ae}(x, y)$ , being modulated by the molecular coherence  $\rho_{ab}$ . For a spatially varying pump laser beam, the coherence becomes position dependent  $\rho_{ab} \rightarrow \rho_{ab}(x, y)$  and plays the role of the intensity-dependent function  $f(x, y)$  of above. For this description to be valid, the spatial variation of  $\rho_{ab}$  must be much slower than the size of the individual dipoles  $\mu_{ae}$  (atomic scale) so that internal states of the molecules are not significantly perturbed (i.e., the energy level structure of Fig. 2 is still a valid description). When driven to near its maximum value of  $\rho_{ab} = 0.5$  by the intense pump and Stokes laser beams, the coherence may exhibit spatial structures much smaller than the wavelength of light. Because we will study a strongly driven molecular system with realistic parameters, analytical techniques do not adequately describe the system, and a numerical approach is needed. The coherence can be found by solving the density matrix equations that describe the time evolution of the system [33]:

$$\begin{aligned} \frac{\partial \rho_{ab}}{\partial t} &= -\left(\frac{\gamma}{2} + \gamma_d\right)\rho_{ab} + i\left(\frac{A}{2} - \frac{D}{2} + \Delta\omega\right)\rho_{ab} \\ &\quad + i\frac{B}{2}(\rho_{bb} - \rho_{aa}), \\ \frac{\partial \rho_{bb}}{\partial t} &= -\gamma\rho_{bb} - \text{Im}\{B^*\rho_{ab}\}, \\ \frac{\partial \rho_{aa}}{\partial t} &= \gamma\rho_{bb} + \text{Im}\{B^*\rho_{ab}\}. \end{aligned} \quad (9)$$

Here  $B = E_P E_S^* \mu_{ae} \mu_{be}^* / (2\Delta\omega \hbar^2)$  is the two photon Rabi frequency,  $\Delta\omega$  is the two-photon detuning from the Raman transition, and  $A$  and  $D$  are the Stark shifts of the relevant levels due to the intense pump and Stokes laser beams. The quantity  $\gamma$  is the population decay rate from the excited Raman level to the ground level, and  $\gamma_d$  is the dephasing rate of the molecular coherence due to processes that do not alter population levels. Within the approximation that the single-photon detunings are much larger than the other rates in the problem, Eqs. (9) are exact, and they include effects such as power broadening and the saturation of the Raman transition.

We proceed with a numerical calculation for a model molecular system with parameters similar to those of recent CARS experiments [13–16]. We consider a pump laser beam at a wavelength of  $\lambda_P = 1 \mu\text{m}$  and a hypothetical  $X-Y$  molecular vibration with a Raman transition frequency of  $1000 \text{ cm}^{-1}$ . As above, for simplicity, we take the wavelength of the scattered light to be the same as the pump laser wavelength,  $\lambda_G = \lambda_P$ . We take the detuning of the beams from the excited electronic level to be  $\Delta_P = 10000 \text{ cm}^{-1}$  and assume a dipole matrix element of 1 atomic unit for both the  $|a\rangle \rightarrow |e\rangle$  and  $|b\rangle \rightarrow |e\rangle$  transitions. We take the decay rate from the excited Raman level to the ground level to be  $\gamma = 2\pi \times 1 \text{ cm}^{-1}$  (i.e., frequency width of 30 GHz). For simplicity and clarity, we focus on one spatial dimension  $x$  and assume a standing wave pump beam and a spatially uniform Stokes laser beam. We take these two beams to be produced by  $Q$ -switched pulsed lasers with 10 ns duration and with a flat-top temporal profile. We take the beams to be focused to an area of  $1 \mu\text{m} \times 1 \mu\text{m}$  using a microscope objective lens. We numerically solve Eqs. (9) with the initial condition that the molecular system starts in the ground level,  $\rho_{aa}(t = 0) = 1$ ,  $\rho_{bb}(t = 0) = 0$ , and  $\rho_{ab}(t = 0) = 0$ .

The solid line in Fig. 3 shows the numerically calculated coherence versus time at the peak of the pump standing wave and for a pulse energy of  $1.5 \mu\text{J}$  (per 10-ns-long pulse) for both the pump and the Stokes laser beams (corresponding to

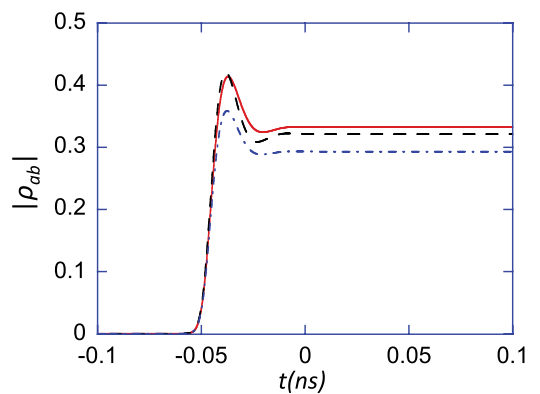


FIG. 3. (Color online) Solid line shows evolution of coherence at peak of standing-wave pump profile for pulse energy of  $1.5 \mu\text{J}$  (per 10-ns-long pulse) for both pump and Stokes laser beams. After some initial time dynamics, the coherence settles to a value of  $|\rho_{ab}| = 0.33$ . The dashed line is the numerically calculated coherence for 10% higher laser intensities. In the simulation of the dotted-dashed line, the total dephasing rate for the molecular coherence is increased by 40%. All three results agree reasonably well, demonstrating the robustness of the coherence preparation.

an intensity of  $15 \text{ GW/cm}^2$  for each laser). In this calculation, we turn on the laser beams in 10 ps, take  $\Delta\omega = 0$ , and assume the ideal case of  $\gamma_d = 0$ . After significant temporal dynamics, the coherence reaches a steady-state value of  $|\rho_{ab}| = 0.33$ . We have tested the sensitivity of the scheme to variations in experimental parameters and have found the results to be relatively robust against perturbations. For example, the dashed line in Fig. 3 shows the evolution of the coherence for 10% higher laser intensities (i.e.,  $1.65 \mu\text{J}$  per pulse for each beam). The dotted-dashed line is the coherence where we have an additional dephasing rate of  $\gamma_d = 2\pi \times 0.2 \text{ cm}^{-1}$  (i.e., the total dephasing linewidth for the molecular coherence is increased by 40%). For both cases, the results are reasonably close to the results of the original simulation, showing the robustness of the coherence preparation.

In Fig. 4, we repeat the time domain simulations of Fig. 3 at each point along the spatial profile of the standing-wave

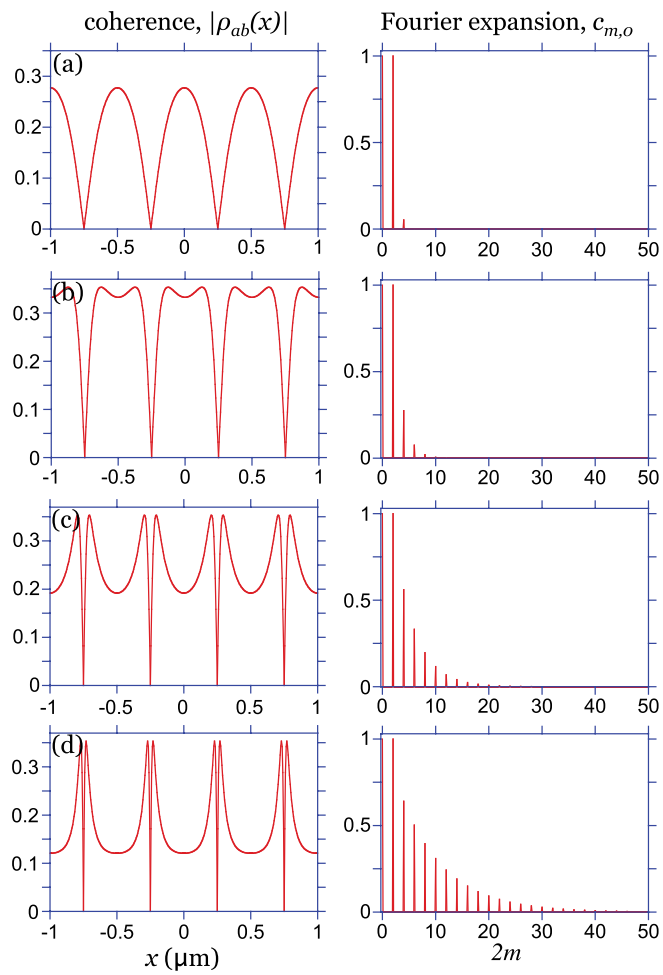


FIG. 4. (Color online) Molecular coherence  $\rho_{ab}(x)$  and its normalized Fourier series expansion coefficients  $c_{m,0}$  as pump and Stokes laser intensities are increased. Here we numerically solve the density matrix equations (9) for flat-top 10-ns-long pump and Stokes laser pulses and calculate the coherence at each spatial point along the standing-wave profile of the pump laser beam. For parts (a) through (d), the pulse energies are 0.5, 1.5, 4, and  $10 \mu\text{J}$  (per 10-ns-long pulse) for both laser beams, respectively. For part (d), the Fourier series coefficients extend out to about  $40\kappa$  which results in a corresponding factor of 40 in the resolution enhancement.

pump laser beam and record the values of the established coherence after the system reaches steady state. The plots show the numerically calculated coherence,  $\rho_{ab}(x)$ , and its normalized Fourier series expansion coefficients,  $c_{m,0}$ , for varying levels of pump and Stokes laser intensities. For parts (a) through (d), the pulse energies are  $0.5 \mu\text{J}$ ,  $1.5 \mu\text{J}$ ,  $4 \mu\text{J}$ , and  $10 \mu\text{J}$  (per 10-ns-long pulse) for both laser beams, respectively. These energy levels are easily generated by Q-switched pulsed lasers, and the intensities achieved at the focus are comparable to intensities used in typical CARS experiments [13,34]. As expected, increased pulse energies produce spatial structures in the molecular coherence that are much smaller than the wavelength of the pump light. The drop in the coherence near the intensity peaks of the standing wave profile is due to the saturation of the Raman transition. The Fourier series expansion plots in the right-hand side of Fig. 4 shows how far the spatial frequencies extend in units of  $\kappa$ . For part (d), assuming an experimental signal to noise ratio of about 20, the coefficients extend out to about  $2m \approx 40$  (i.e., the spatial frequencies extend to about  $40\kappa$ ), which would result in a corresponding factor of 40 in the resolution enhancement.

We next discuss sweeping the intensity of the pump laser beam with a speed  $v_x$  to produce the spatiotemporal modulation. For this purpose, we numerically integrate Eqs. (9) at a fixed position in space and calculate the coherence as the standing-wave pump laser profile is swept. Figure 5 shows the calculated coherence vs time for an energy of  $10 \mu\text{J}$  per pulse for both laser beams [i.e., for conditions of the numerical simulation of Fig. 4(d)]. We choose the speed  $v_x$  such that the frequency shift between adjacent orders is  $2\delta\omega_x = 2\pi \times 1 \text{ GHz}$ . The coherence calculation of Fig. 5 closely replicates the spatial structure of Fig. 4(d), demonstrating that by sweeping the standing-wave pump pattern, we roughly establish a traveling-wave pattern  $\rho_{ab}(x - v_x t)$ , as required by the scheme. We note that, for this procedure to work, it is critical that steady state in the integration of Eqs. (9) is achieved at time scales much faster than the time variation of the pump field as a result of the sweep. This, in turn, requires  $\delta\omega_x \ll \gamma$ , which is satisfied for the numerical calculation of Fig. 5.

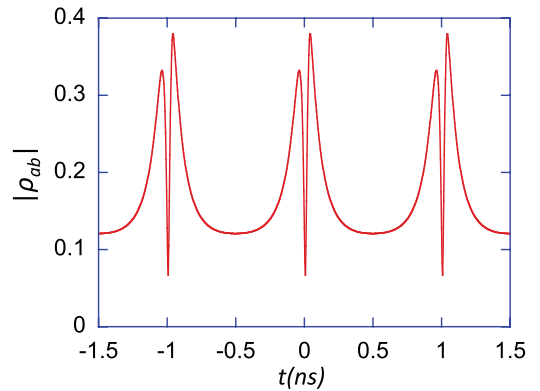


FIG. 5. (Color online) Coherence vs time as standing-wave pump laser is swept for energy of  $10 \mu\text{J}$  per pulse for each laser beam. The coherence reasonably replicates the spatial structure of Fig. 4(d), demonstrating that a traveling-wave pattern of  $\rho_{ab}(x - v_x t)$  is established.

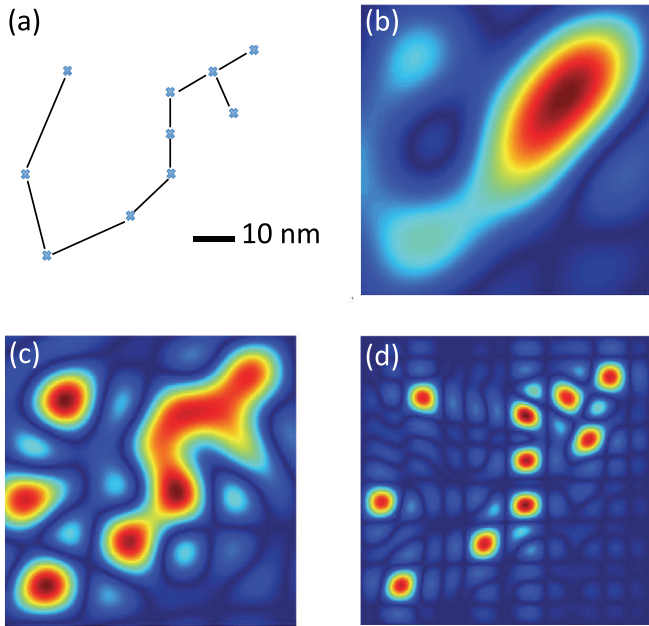


FIG. 6. (Color online) (a) Hypothetical complex molecular structure where the positions of the vibrational resonance are indicated with crosses. (b) Reconstructed image where Fourier series expansion of coherence extends out to  $24\kappa$ . The spatial frequencies in the region  $-24\kappa < k_x < 24\kappa$  and  $-24\kappa < k_y < 24\kappa$  are recovered and contribute to the image. In parts (c) and (d), the coherence extends to  $50\kappa$  and  $100\kappa$  in the Fourier space, respectively. For all cases, the imaging is performed with scattered CARS light at a wavelength of  $\lambda_G = 1 \mu\text{m}$ .

We next present a calculation that shows the effect of enhanced resolution on the image. For this purpose, we consider a hypothetical complex molecular structure that is shown in Fig. 6(a), where the positions with the  $X$ - $Y$  bond that exhibit vibrations are indicated. Because the molecular structure is at the 10 nm scale and the wavelength of scattered light is  $1 \mu\text{m}$ , traditional imaging techniques cannot resolve the relevant features. Figure 6(b) shows the reconstructed image where the Fourier series expansion of the coherence extends out to  $24\kappa$ , and therefore in the image plane the spatial frequencies  $-24\kappa < k_x < 24\kappa$  and  $-24\kappa < k_y < 24\kappa$  are maintained (i.e., the resolution is enhanced by a factor of 24). Various features of the spatial structure are already resolved with this enhancement. In Figs. 6(c) and 6(d), we calculate the image with resolution enhancement factors of 50

and 100, respectively. In Fig. 6(d), almost all relevant features of the complex structure are resolved. For the conditions of the numerical calculation of Fig. 4, the results of Figs. 6(b) through 6(d) would be obtained for pump and Stokes pulse energies of about  $4 \mu\text{J}$ ,  $10 \mu\text{J}$ , and  $40 \mu\text{J}$  per pulse, respectively.

One of the key drawbacks of the scheme is the long integration time required by the low signal levels. By choosing the parameters of the mixing beam appropriately, photon scattering rates from a single molecule at the generated frequency of  $\omega_G$  that exceed 1 MHz can likely be achieved. Assuming 10% photon collection efficiency, a  $30 \text{ pixel} \times 30 \text{ pixel}$  image, and a resolution enhancement of 30 (producing  $30 \times 30 = 900$  different frequencies that need to be resolved), we would then have roughly a single collected photon per second per pixel at each frequency. Obtaining a good signal-to-noise ratio would then require many minutes of integration. Due to such long integration times, implementing our approach will likely require stationary molecular samples where the motion is negligible during the relevant time scales.

In conclusion, we have suggested a different approach for optical imaging that has the potential to achieve nanoscale resolution in the far field. The approach relies on using optical nonlinearities to mix down high spatial frequency components into the propagating region. These components are then recovered in the image plane using an alternative type of spatiotemporal modulation. As mentioned above, the main motivation for this work is the possibility of nanoscale imaging of complex molecular structures. Although we have focused on a CARS nonlinearity, the approach is general and can likely be implemented using other nonlinear optical processes. We note that there are a number of important issues that we have not addressed in this manuscript. (i) We have assumed that the scattered light is collected with an ideal microscope objective that has a numerical aperture of  $\text{NA} = 1$ . We have not presented a detailed analysis of image formation through a real system. (ii) In our CARS analysis, we have not included the contribution of other nonlinear processes such as nonresonant four-wave mixing. (iii) We have not addressed the issues related to the possible optical damage to the molecule. A detailed study of these issues will be among our future investigations.

We thank Josh Weber, Dan Sikes, Nick Proite, and Jared Miles for helpful discussions. This work was partially supported by the Air Force Office of Scientific Research (AFOSR) and the Wisconsin Alumni Research Foundation (WARF).

- 
- [1] E. Betzig, *Opt. Lett.* **20**, 237 (1995).
  - [2] C. Hettich, C. Schmitt, J. Zitzmann, S. Kuhn, I. Gerhardt, and V. Sandoghdar, *Science* **298**, 385 (2002).
  - [3] A. N. Boto, P. Kok, D. S. Abrams, S. L. Braunstein, C. P. Williams, and J. P. Dowling, *Phys. Rev. Lett.* **85**, 2733 (2000).
  - [4] M. D'Angelo, M. V. Chekhova, and Y. Shih, *Phys. Rev. Lett.* **87**, 013602 (2001).
  - [5] K. S. Johnson, J. H. Thywissen, N. H. Dekker, K. K. Berggren, A. P. Chu, R. Younkin, and M. Prentiss, *Science* **280**, 1853 (1998).
  - [6] S. J. Bentley and R. W. Boyd, *Opt. Express* **12**, 5735 (2004).
  - [7] J. B. Pendry, *Phys. Rev. Lett.* **85**, 3966 (2000).
  - [8] S. W. Hell and J. Wichmann, *Opt. Lett.* **19**, 780 (1994).
  - [9] V. Westphal and S. W. Hell, *Phys. Rev. Lett.* **94**, 143903 (2005).
  - [10] D. Wildanger, J. R. Maze, and S. W. Hell, *Phys. Rev. Lett.* **107**, 017601 (2011).
  - [11] M. G. L. Gustaffson, *J. Microsc.* **198**, 82 (2000).
  - [12] M. G. L. Gustaffson, *Proc. Natl. Acad. Sci. USA* **102**, 13081 (2005).

- [13] J. X. Cheng, A. Volkmer, and X. S. Xie, *J. Opt. Soc. Am. B* **19**, 1363 (2002).
- [14] F. El-Diasty, *Vib. Spectrosc.* **55**, 1 (2011).
- [15] F. Ganikhhanov, C. L. Evans, B. G. Saar, and X. S. Xie, *Opt. Lett.* **31**, 1872 (2006).
- [16] C. L. Evans, X. Xu, S. Kesari, X. S. Xie, S. T. C. Wong, and G. S. Young, *Opt. Express* **15**, 12076 (2007).
- [17] K. M. Hajek, B. Littleton, D. Turk, T. J. McIntyre, and H. Rubinsztein-Dunlop, *Opt. Express* **18**, 19263 (2010).
- [18] W. P. Beeker, P. Gross, C. J. Lee, C. Cleff, H. L. Offerhaus, C. Fallnich, J. L. Herek, and K.-J. Boller, *Opt. Express* **17**, 22632 (2009).
- [19] W. Liu and H. Niu, *Phys. Rev. A* **83**, 023830 (2011).
- [20] J. Lu, W. Min, J. Conchello, X. S. Xie, and J. W. Lichtman, *Nano Lett.* **9**(11), 3883 (2009).
- [21] J. E. Thomas, *Opt. Lett.* **14**, 1186 (1989).
- [22] F. Le Kien, G. Rempe, W. P. Schleich, and M. S. Zubairy, *Phys. Rev. A* **56**, 2972 (1997).
- [23] S. Qamar, S. Y. Zhu, and M. S. Zubairy, *Phys. Rev. A* **61**, 063806 (2000).
- [24] E. Paspalakis and P. L. Knight, *Phys. Rev. A* **63**, 065802 (2001).
- [25] G. S. Agarwal and K. T. Kapale, *J. Phys. B* **39**, 3437 (2006).
- [26] D. D. Yavuz and N. A. Proite, *Phys. Rev. A* **76**, 041802(R) (2007).
- [27] A. V. Gorshkov, L. Jiang, M. Greiner, P. Zoller, and M. D. Lukin, *Phys. Rev. Lett.* **100**, 093005 (2008).
- [28] K. D. Stokes, C. Schnurr, J. R. Gardner, M. Marable, G. R. Welsch, and J. E. Thomas, *Phys. Rev. Lett.* **67**, 1997 (1991).
- [29] J. R. Gardner, M. L. Marable, G. R. Welsch, and J. E. Thomas, *Phys. Rev. Lett.* **70**, 3404 (1993).
- [30] H. Li, V. A. Sautenkov, M. M. Kash, A. V. Sokolov, G. R. Welch, Y. V. Rostovtsev, M. S. Zubairy, and M. O. Scully, *Phys. Rev. A* **78**, 013803 (2008).
- [31] N. A. Proite, Z. J. Simmons, and D. D. Yavuz, *Phys. Rev. A* **83**, 041803(R) (2011).
- [32] S. E. Harris and A. V. Sokolov, *Phys. Rev. A* **55**, R4019 (1997).
- [33] D. D. Yavuz, A. V. Sokolov, and S. E. Harris, *Phys. Rev. Lett.* **84**, 75 (2000).
- [34] A. A. Oraevsky, L. B. Da Silva, A. M. Rubenchik, M. D. Feit, M. E. Glinsky, M. D. Perry, B. M. Mammini, W. Small, IV, and B. C. Stuart, *IEEE J. Sel. Top. Quantum Electron.* **2**, 801 (1996).